Itinerant ferromagnetism in van der Waals $Fe_{5-x}GeTe_2$ crystals above room temperature

Hongrui Zhang,[1,*] Rui Chen,[1,6] Kun Zhai,[2] Xiang Chen,[3] Lucas Caretta,[1] Xiaoxi Huang,[1] Rajesh V. Chopdekar,[4] Jinhua Cao,[1,6] Jirong Sun,[5] Jie Yao,[1,6] Robert Birgeneau,[1,3] and Ramamoorthy Ramesh[1,3,†]

[1]*Department of Materials Science and Engineering, University of California, Berkeley, California 94720, USA*

[2]*Center for High Pressure Science (CHiPs), State Key Laboratory of Metastable Materials Science and Technology, Yanshan University, Qinhuangdao 066004, People's Republic of China*

[3]*Department of Physics, University of California, Berkeley, California 94720, USA*

[4]*Advanced Light Source, Lawrence Berkeley National Laboratory, Berkeley, California 94720, USA*

[5]*Beijing National Laboratory for Condensed Matter Physics, Institute of Physics, Chinese Academy of Sciences, Beijing 100190, People's Republic of China*

[6]*Materials Sciences Division, Lawrence Berkeley National Laboratory, Berkeley, California 94720, USA*

(Received 15 May 2020; accepted 1 July 2020; published 19 August 2020)

Two-dimensional (2D) van der Waals (vdW) magnets have recently attracted increasing attention, as they provide a novel system for exploring 2D magnetism. However, intrinsic ferromagnetism in 2D systems has almost exclusively been observed at low temperatures, limiting their technological relevance. Fe_NGeTe_2 ($N = 3$, 4, and 5) systems are currently becoming the most attractive 2D vdW materials due to their relatively high Curie temperatures and large saturation magnetization. However, the nature of their complex yet intriguing magnetic behaviors is still unclear, in part due to the multiple inequivalent iron sites and iron vacancies. Here, we show evolution of magnetic ordering transitions in $Fe_{5-x}GeTe_2$ with high Curie temperature and a strong saturation magnetization using photoemission electron microscopy and transport measurements. At 275 K, the ferromagnet transitions to a ferrimagnet, and below 110 K transitions to a state with glassy clusters. These are evidenced from temperature-dependent magnetic stripe domain evolution and anisotropic magnetoresistance measurements. Our findings show a clear magnetic ground state of $Fe_{5-x}GeTe_2$ at room temperature which signals that $Fe_{5-x}GeTe_2$ system is a very promising candidate for spintronic devices and provides a material design pathway to further increase the Curie temperature and saturation moments in vdW ferromagnets.

DOI: 10.1103/PhysRevB.102.064417

Two-dimensional (2D) van der Waals (vdW) ferromagnetic materials offer a new magnetic engineering platform that allows for the arbitrary assembly of layered heterostructures. This has triggered immense research on exploring new phenomena and designing novel spintronic devices with tailored functionalities. In recent years, many bulk vdW ferromagnets have been discovered, such as $Cr(Ge, Si)Te_3$ [1–3], $Cr(I, Br, Cl)_3$ [4–6], $(Mn_{1/3}, Fe_{1/4}, Cr_{1/3})TaS_2$ [7–9], and Fe_3GeTe_2 [10–13]. In the 2D limit, strong magnetic anisotropy enables the stabilization of a long-range magnetic order, despite enhanced thermal fluctuations. Such 2D magnets are atomically thin $CrGeTe_3$ [14], CrI_3 [15], and Fe_3GeTe_2 [16], with intrinsic ferromagnetism up to 30, 40, and 150 K, respectively. Stabilization of such monolayers has made it possible to push 2D materials-based spintronic devices to higher speeds and lower energy consumption [17–19].

Among these systems, Fe_3GeTe_2 is an itinerant Heisenberg ferromagnet that has a high bulk Curie temperature ($T_c = 230$ K) and perpendicular magnetic anisotropy (PMA). Moreover, its T_c can be enhanced up to room temperature by ionic liquid gating [20] or patterning methods [21,22]. These desirable properties have sparked intense research in Fe_3GeTe_2-based spintronic devices; for instance, a giant tunneling magnetoresistance of 160% has been observed in Fe_3GeTe_2/h-BN/Fe_3GeTe_2 heterostructures [23]. In addition, a variety of spin-orbit phenomena has recently emerged in 2D spintronics. For example, perpendicular magnetization switching was driven via a spin-orbit torque in a bilayer Pt/Fe_3GeTe_2 device [24,25]. Moreover, topological magnetic solitons, such as vortex phases [21], skyrmion bubbles [26], and Néel-type skyrmion [27] have been observed in Fe_3GeTe_2 single crystals and heterostructures. In short, Fe_3GeTe_2 is currently the most promising candidate for manipulating spins and spin textures; however, further efforts are required to enhance the T_c up to room temperature. Very recently, vdW Fe_4GeTe_2 and $Fe_{5-x}GeTe_2$ phases have been synthesized displaying intrinsic ferromagnetism. Due, in part, to higher Fe concentrations in such systems, they exhibit an enhanced Curie temperature near room temperature (270–310 K) and a larger saturation magnetization (500-640 emu/cm^3) [28–31]. Additionally, $Fe_{5-x}GeTe_2$ single crystals show very complex magnetic behavior because of tunable iron content and iron vacancies. To date, the exact magnetic ground state(s) of $Fe_{5-x}GeTe_2$ has remained an open question, which is a key to the search for 2D vdW ferromagnetic materials with high Curie temperature. In this paper, we investigate the fascinating magnetic and electronic properties of $Fe_{5-x}GeTe_2$ nanoflakes and single crystals in detail from both micro-

*hongruizhang@berkeley.edu
†rramesh@berkeley.edu

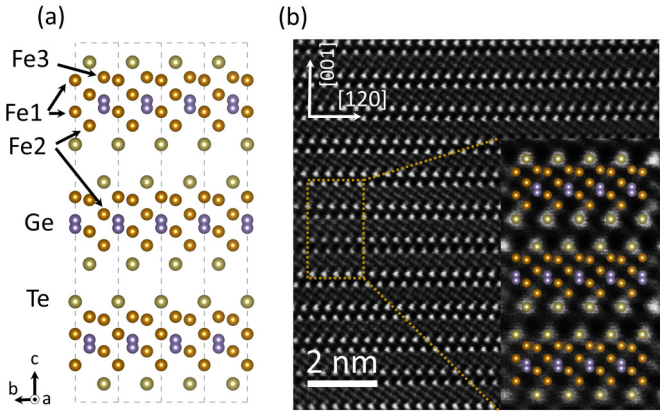

FIG. 1. Structural characterization of the $Fe_{5-x}GeTe_2$ single crystal. (a) Crystal structure of $Fe_{5-x}GeTe_2$ (side view, one unit cell). (b) High-angle annular dark-field STEM image of the cross section of $Fe_{5-x}GeTe_2$. Inset: Magnified image of one unit cell with the atoms overlaid on top to demonstrate the layered structure of $Fe_{5-x}GeTe_2$.

and macroperspectives using a combination of magnetization measurements, x-ray magnetic circular dichroism photoemission electron microscopy (XMCD-PEEM) and magnetotransport measurements. Our experimental results reveal a robust in-plane magnetic anisotropy, rather than the perpendicular anisotropy reported in the previous Fe_NGeTe_2 systems. Furthermore, both magnetic and transport measurements indicate two intriguing magnetic-phase transitions upon cooling below room temperature: a ferromagnetic state that transitions to ferrimagnetic state just below room temperature (about 275 K), and further evolves to a state with glassy clusters at lower temperatures (below 110 K).

$Fe_{5-x}GeTe_2$ adopts a trigonal crystal structure with space group $R3m$ [29]. Figure 1(a) shows the side view of the crystal structure, where nonequivalent Fe sites are labeled as Fe1, Fe2, and Fe3. The unit cell of $Fe_{5-x}GeTe_2$ is composed of three similar blocks, each of which consists of four magnetic monolayers sandwiched by Te monolayers, including a honeycomb Fe1/Fe3 layer and a weakly bonded Fe_3Ge layer (see Supplemental Material [32], Fig. S1). Notably, it is the additional Fe1 and Fe3 layer that distinguishes the structural and magnetic properties of $Fe_{5-x}GeTe_2$ from those of Fe_3GeTe_2.

We successfully synthesized high-quality $Fe_{5-x}GeTe_2$ single crystals using a chemical vapor transport method (See Supplemental Materials [32], Method section). Energy-dispersive x-ray spectroscopy revealed that the stoichiometry of Fe in $Fe_{5-x}GeTe_2$ is 4.96 ($x = 0.04$), which is higher than previously reported values [28,29,33]. The $\theta - 2\theta$ symmetric scan of $Fe_{5-x}GeTe_2$ single crystal shows only $(00l)$ Bragg peaks, which demonstrates that the surface of the crystal is the *ab* plane. (see Supplemental Material [32], Fig. S2) As the Fe concentration increases, the volume and *c*-lattice parameter increase correspondingly. The *c*-lattice parameter calculated from x-ray diffraction (XRD) is 29.26 Å, which is higher than that of previously reported results [28,29,33]. Figure 1(b) shows a *Z*-contrast scanning transmission electron microscopy (STEM) image along the [110] direction, which agrees well with the layered schematic crystal structure shown

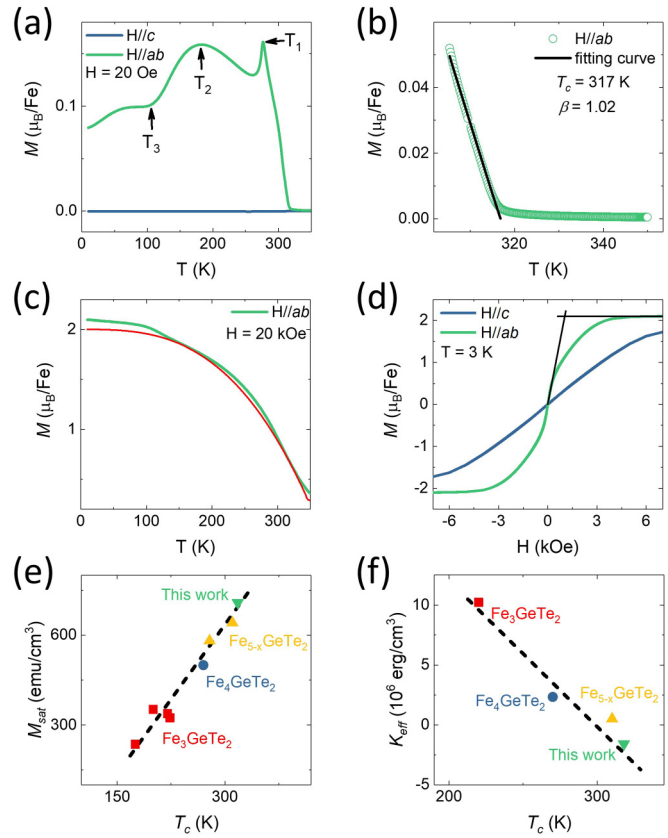

FIG. 2. Magnetization measurement of $Fe_{5-x}GeTe_2$ single crystals. Temperature-dependent magnetization curves of $Fe_{5-x}GeTe_2$ single crystals under a magnetic field of 20 Oe (a) and 20 kOe (c) along the *ab* plane and *c* axis. The red curve is the result of fitting to the standard Bloch spin-wave model [35]. (b) Temperature-dependent magnetization curves near the T_c fit by the mean-field model. Isothermal magnetization curves of $Fe_{5-x}GeTe_2$ single crystals at 3 K (d) along the *ab* plane and *c* axis. Curie temperature T_c-dependent saturation magnetization M_{sat} (e) and uniaxial magnetic anisotropy energy K_{eff} (f) for Fe_3GeTe_2 [10,12,13], Fe_4GeTe_2, [31] and $Fe_{5-x}GeTe_2$ [28,29] ferromagnets.

in the inset of Fig. 1(b). The strong contrast originates from the heavy Te atom layers, whereas the weaker contrast originates from the lighter Fe- and Ge-based layers. Clear vdW gaps between the $Fe_{5-x}GeTe_2$ sublayers show a perfectly layered nature, which verifies the high quality of the synthesized single crystals.

Figure 2(a) reveals the temperature-dependent magnetization (M-T) of the bulk $Fe_{5-x}GeTe_2$ single crystal acquired using a superconducting quantum interference device, under an external magnetic field $H = 20$ Oe. The out-of-plane magnetization ($H//c$) is much smaller at all temperatures. In contrast, the in-plane ($H//ab$)M-T data show several unique features. The magnetization increases sharply as the temperature decreases and crosses the transition temperature T_c (~317 K), indicating a paramagnetic to ferromagnetic transition. Based on mean-field model, the spontaneous magnetization (M_S) should show a power-law dependence on the reduced temperature, $M_S(T) \propto (T_c - T)^{\beta}$. The magnetization data near T_c can be fit well with this model, and the parameters are $T_c = 317$ K and $\beta = 1.02$, as shown in Fig. 2(b). The

critical exponent β of $Fe_{5-x}GeTe_2$ is far larger than that of Fe_3GeTe_2 (0.37) [34] and the mean-field theory value (0.5). Additionally, there are three bumps observed in the *M-T* curve, which are marked as T_1 (275 K), T_2 (180 K), and T_3 (110 K). Interestingly, during the same field-cooling measurement with a higher magnetic field of $H = 1$ kOe, T_1 vanishes from the *M-T* curve, while T_2 shifts to a slightly lower temperature (148 K; see Supplemental Material [32], Fig S3). When the applied field is further increased to 20 kOe, both T_1 and T_2 disappear from the *M-T* curve, as shown in Fig. 2(c). These unconventional features around T_1 and T_2 likely suggest that the varying magnetic ground states below $T = 275$ K are a result of nonunidirectional magnetic moments between the monolayers of $Fe_{5-x}GeTe_2$, which are then aligned parallel under larger magnetic fields. In order to gain more insights into the ferromagnetic behavior, we fit the *M-T* data at 20 kOe with the standard Bloch spin-wave model [35], $M = M_0\ (1 - BT^{\eta})$, where M_0, B, and η are the saturation magnetization, the Bloch constant, and the Bloch exponent, respectively. Overall the experimental data fit the model well, except for an anomalous increase of the magnetization below 110 K. We attribute the increased bulk magnetization to the reduction of lattice constant along the c axis driven by coupling of the lattice to the magnetism [28], leading to an enhanced exchange coupling between the magnetic layers of $Fe_{5-x}GeTe_2$.

Figure 2(d) show the isothermal magnetization (*M-H*) measured as a function of magnetic field H at 3 K. We extract a saturation magnetization (M_{sat}) of $2.1\mu_B$/Fe at 3 K. This saturation magnetization is similar to that of Fe metal and, as expected, is higher than those of Fe_3GeTe_2($1.6\,\mu_B$/Fe) [10] and Fe_4GeTe_2($1.8\,\mu_B$/Fe) [31] single crystals. The *M-H* loops taken along both the *ab* plane and *c* axis illustrate an in-plane anisotropy, in good accord with the *M-T* data. More complicated magnetic behaviors are observed as a function of applied magnetic field in the *ab* plane at 3 K, displaying two distinct slopes before saturation: a large slope is observed at low fields, followed by a gradual decrease of slope until saturation. The lower slope occurring before saturation is possibly induced by the coupling of the lattice to the magnetism at ~110 K [28], above which the two-slope behavior vanishes in *M-H* measurement. (see Supplemental Material [32], Fig. S3) To further elucidate the magnetism of this crystal, we compare magnetic properties between various Fe_NGeTe_2 ($N = 3$, 4, 5) systems. By plotting the saturation magnetization (M_{sat}) versus T_c for various Fe_NGeTe_2 ($N = 3$, 4, 5) crystals, we find that all data lie along the same linear curve, as shown in Fig. 2(e). In our system, the T_c and M_{sat} of $Fe_{5-x}GeTe_2$ single crystals are 317 K and 708 emu/cm^3, respectively, both of which are higher than the recently reported $Fe_{5-x}GeTe_2$ results [28–30]. It is worth mentioning that the magnetic anisotropy is also effectively modulated by the Fe concentration. Fe_3GeTe_2 has PMA, while in previously reported Fe_4GeTe_2 and $Fe_{5-x}GeTe_2$, the magnetic anisotropy lies in the *ab* plane at high temperatures, and rotates to the *c* axis below 110 K [28,30,31]. In contrast, the magnetic anisotropy of $Fe_{5-x}GeTe_2$ is always in the *ab* plane in our case. From the *M-H* curves for $H//c$ and $H//ab$, we estimate that the effective uniaxial magnetic anisotropy (K_{eff}) of $Fe_{5-x}GeTe_2$ is -1.6×10^6 erg/cm^3 at 3 K, where the negative sign signifies the in-plane anisotropy. Meanwhile, a negative correlation is unraveled between T_c and K_{eff} [Fig. 2(f)]. The high T_c results from increased neighboring Fe-Fe exchange interaction, since more Fe is introduced into the system and the number of Fe neighbors is significantly increased.

To help elucidate the complex magnetic behavior, we performed temperature-dependent PEEM imaging on layered $Fe_{5-x}GeTe_2$ nanoflakes produced by standard micromechanical exfoliation onto a SiO_2 substrate. After exfoliation, the native oxide on the sample surface was removed by lightly etching using Ar^+ ions, and 1-nm Pd protection layer is immediately grown on top. The thickness of the nanoflake is about 70 nm, as determined by atomic force microscopy (see Supplemental Material [32], Fig. S4). Figure 3 shows temperature-dependent PEEM images recorded with the photon energy tuned to the Fe L_3 absorption edge (706.3 eV) under magnetic remanence. The contrast in the images is a result of XMCD, and thus bright and dark contrast indicates the local magnetization component parallel and antiparallel to the x-ray direction, respectively. The nanoflake exhibits stripe-shaped magnetic domains, the width of which is about 1.5 to 2μm, marked by red and blue lines. This value is approximately one order of magnitude larger than that of Fe_3GeTe_2 flakes ($\sim 0.15\,\mu$m) with similar flake thickness [21]. This can be attributed to a different magnetic anisotropy between Fe_3GeTe_2 and Fe_5GeTe_2. The shape of domains remains the same as the temperature decreases, and the domain walls are also stationary. Meanwhile, the spin orientation is always in plane, as determined from *M-T* curves. Therefore, we identify no spin reorientation occurring from 120 to 275 K.

It is worth noting that the magnetic contrast increases as the temperature decreases, followed by a maximum at 180 K below which the contrast tends to diminish, particularly at 110 K. This unconventional trend is consistent with the magnitude of the magnetization of the *M-T* curves under low fields as shown in Fig. 3(b). In general, for most ferromagnetic metals, XMCD contrast either increases monotonically or remains constant as the temperature decreases. Thus, the suppressed local magnetization observed here may result from the reversal of some spin orientations or magnetic compensation effects. The magnetic domain contrast almost vanishes at 110 K when the coupling of the lattice to the magnetism occurs [28].

To further explore the fascinating magnetic evolution described above, we performed magnetotransport measurements on a nanoflake of similar thickness (~70 nm). The inset of Fig. 4(a) depicts the optical image of the Hall bar device. Figure 4(a) shows a resistance versus temperature (*R-T*) curve of the device and its first derivative dR/dT, which mostly exhibits typical metallic behavior. However, anomalies are seen in the *R-T* curve at similar temperatures to those in both the magnetic measurements in Fig. 2 and the PEEM imaging measurements in Fig. 3. They are particularly clear in the two peaks in the dR/dT curve, indicated by green arrows. Figure 4(b) shows the results of Hall-effect measurements performed on the nanoflake. At 340 K, the Hall resistance is linear with the magnetic field, corresponding to a normal Hall effect for paramagnetic system. The deduced carrier density is about 4.9×10^{21} cm^{-3} which is determined by the slope of the linear Hall-effect curve. Anomalous Hall effect sets in when

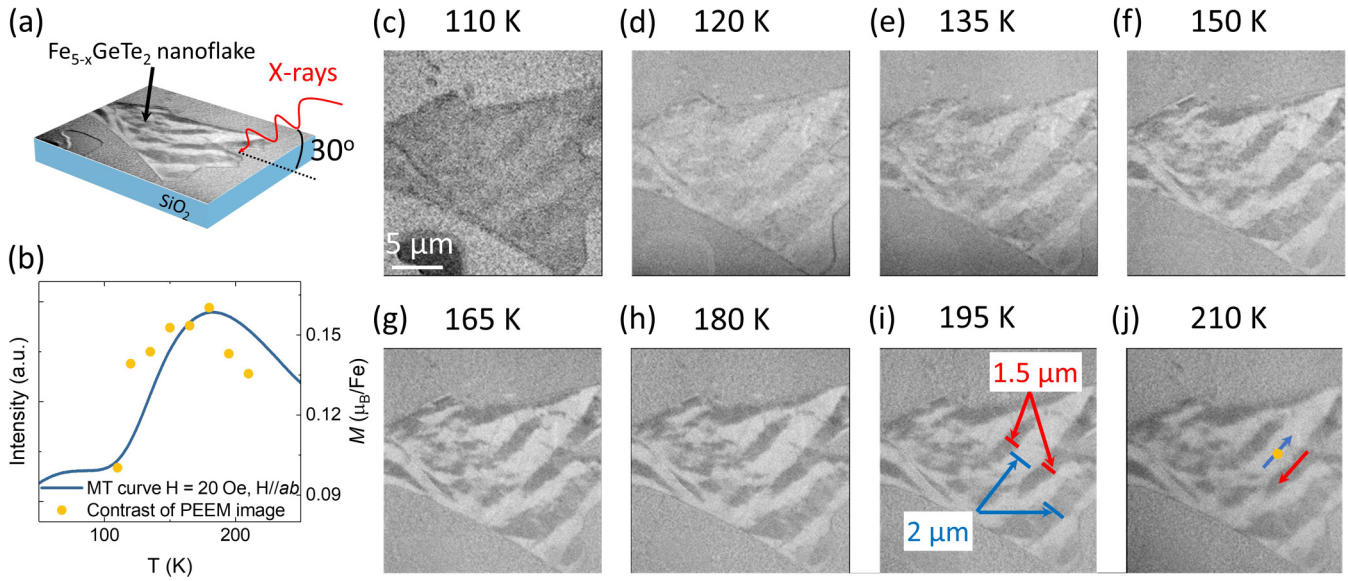

FIG. 3. Temperature-dependent domain imaging of $Fe_{5-x}GeTe_2$ nanoflake. (a) Schematic and experimental geometry of the $Fe_{5-x}GeTe_2$ nanoflake sample. (b) Temperature-dependent magnetization (blue line) and contrast of PEEM imaging (yellow spot) measured at the yellow point in (j). (c)-(j) PEEM image of an $Fe_{5-x}GeTe_2$ flake on a conductive silicon substrate shows the stripe magnetic domain evolution from 110 to 210 K. The width of the magnetic domain is 1.5 and 2 μm, marked by the red and blue lines, respectively.

the temperature is decreased to 320 K and grows continuously with the decreasing temperature until a maximum is obtained at 110 K due to the onset of the transition and the resistance decrease (see Supplemental Material [32], Fig. S5).

Figure 4(d) shows the magnetoresistance (MR) curves of the device at various temperatures, obtained by fixing α, the angle between the in-plane magnetic field H and current I, to 0° and 90°. A butterfly-shaped MR is observed above 120 K, which is a typical feature of ferromagnetic metals (see Supplemental Material [32], Fig. S6) Besides, the MR ratio at 180 K is $\sim-$ 0.06% and 0.07% for $\alpha = 0^o$ and 90°, showing that the MR of the device is greatly anisotropic. However, below 120 K, the shape of the MR curves dramatically changes. A sharp MR peak instead of butterfly-shaped

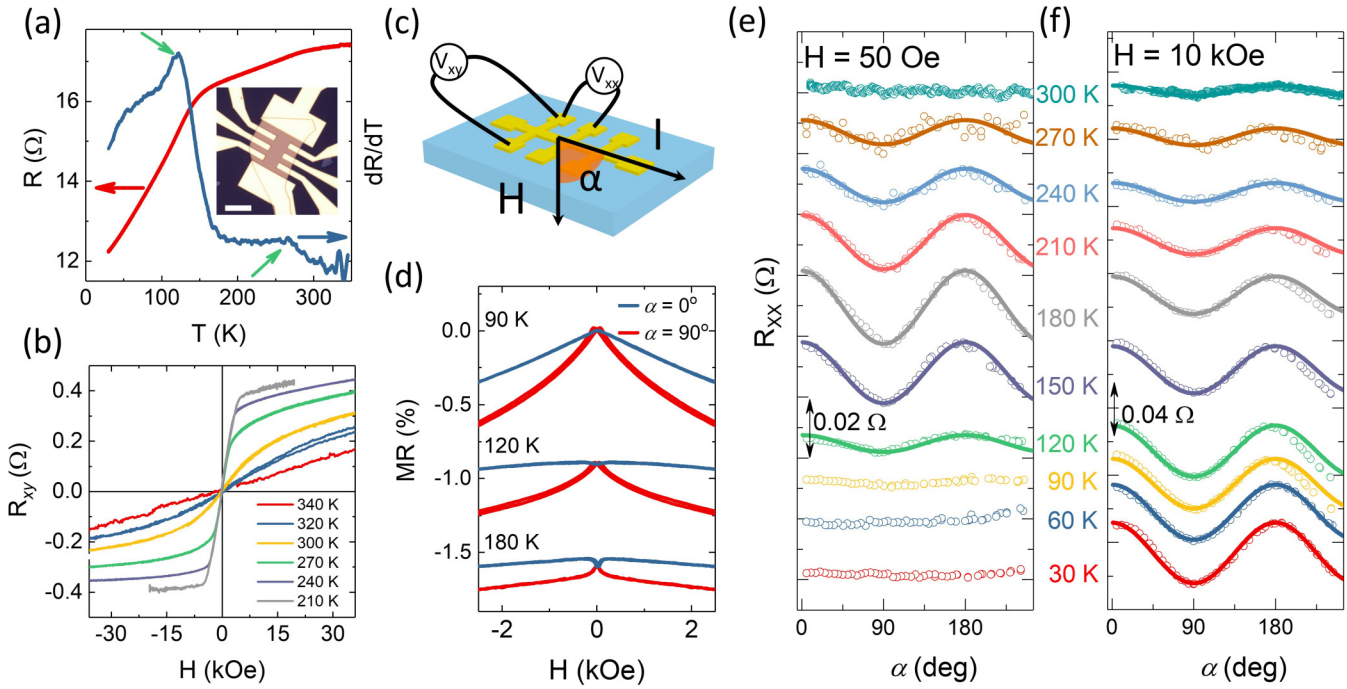

FIG. 4. Transport measurement of $Fe_{5-x}GeTe_2$ nanoflake. (a) Temperature dependence of resistance (red line) and differential resistance with temperature (blue line) for $Fe_{5-x}GeTe_2$ nanoflake. Inset: the optical image of a typical Hall bar device of $Fe_{5-x}GeTe_2$ nanoflake. The scale bar is 10 μm. (b) Anomalous Hall effect at different temperatures. (c) Schematic of anisotropic magnetoresistance; α angle is between current and magnetic field along *ab* plane. (d) Magnetoresistance curve at different temperatures, $\alpha = 0°$. Anisotropic magnetoresistance with the magnetic field scanned within the *ab* plane at different temperatures. The applied magnetic field is 50 Oe (e) and 10 kOe (f).

curves is observed around $H = 0$ Oe. Moreover, the system shows negative magnetoresistance when α is either 0° or 90°. MR value displays a remarkable increase in comparison to the high-temperature cases. At 90 K, the MR ratio increases to -0.28% for $\alpha = 0^\circ$ and -0.54% for $\alpha = 90^\circ$ under a field of 2 kOe. The probability of spin-dependent scattering increases, leading to a corresponding change in negative MR. These features are generally observed in a granular magnetic system [36,37] or superparamagnetic system [38], indicating that the $Fe_{5-x}GeTe_2$ system shows glassy clusters behavior at low temperatures and low magnetic field. Consistent evidence for a glassy clusters state is also obtained by the anisotropic magnetoresistance (AMR) measurements. Figure 4(e) shows the magnetoresistance as a function of angle α at various temperatures. Here, the applied magnetic field H is fixed at 50 Oe, which is larger than the coercive field, such that the magnetization of the material will be aligned with the field. Above 120 K, the R_{xx} shows 180° periodic angular dependence, which can be well fitted using the equation $R_{xx} = R_\perp - \Delta R_{AMR}\cos^2\alpha$, where $\Delta R_{AMR} = R_\perp - R_{//}$, $R_\perp$ and $R_{//}$ correspond to $\alpha = 90^\circ$ and 0°, respectively. This is a typical feature of a ferromagnetic or ferrimagnetic metal. This means that the AMR signal above 120 K is typical of a ferromagnetic metal. The magnetization decreases at 275 K observed in Fig, 2(a) could be attributed to ferrimagnetism or small canting of the ferromagnetic moment. Here, we may exclude the contribution from the magnetic structure with large canting contribution, since we found no MR components along a canted angle, as expected for canted moment system [39] [see Fig. 4(e)]. Therefore, this AMR signal indicates that some spins are oriented in opposite directions. Namely, a ferrimagnetic phase yields such behavior in *M-T* curves and PEEM images from 270 to 135 K. Conversely, below $T = 120$ K, the AMR signal gradually drops to zero, despite a nonzero magnetic field applied. This suppressed AMR behavior at low temperatures indicates the lack of the intrinsic long-range magnetic order at low temperatures, possibly because of the enhanced exchange coupling between interlayer irons due to the strong coupling of the lattice to the magnetism below 110 K. However, once the magnetic field is increased to the saturation field [Fig. 4(f)], the spins are fully aligned with the external field, thus leading to a normal AMR signal.

Finally, we systemically analyze the magnetic ground states of $Fe_{5-x}GeTe_2$ at different temperatures, combining all experimental evidence. The transition from paramagnetic to ferromagnetic phase occurs at 317 K. Then, some spins in one or more Fe sites flip their orientations and induce a sudden drop of magnetization at 270 K. Therefore, it enters the ferrimagnetic state, although we cannot rule out the possibility of the state with small canting or some other exotic ground states. Below 110 K, due to the enhanced magnetic coupling between the honeycomb Fe1/Fe3 layer and Fe_3Ge layer because of the lattice compression, the magnetic ground state is glassy clusters and the saturation magnetization is enhanced. From Fe_3GeTe_2 to Fe_5GeTe_2, the pronounced change is that the additional two iron atoms that form one honeycomb layer are intercalated into the original Fe_3GeTe_2 lattice, leading to the three dramatic observations as follows. First, the Curie temperature is enhanced from 220 to 317 K in the single crystals. Second, the saturation magnetization increases significantly from 338 to 708 emu/cm^3. Last but not least, the crystal favors an in-plane easy magnetization with more iron contents at all temperatures up to T_c. There is currently no theory predicting an upper limit of the magnetic performance as the iron content increases. For instance, as predicted, the stoichiometry of Fe can be further increased above 6, with a vdW phase of Fe_NGeTe_2 dynamically stabilized [31]. Thus, it is very promising that Fe_NGeTe_2 systems can be a candidate material to adopt a higher conductivity, larger magnetization, and T_c far beyond the room temperature. Moreover, Fe_5GeTe_2 has abundant magnetic transitions, strongly suggesting that it is a good system for the investigation into novel topological magnetic structures.

Future studies will be focused on the manipulation of magnetic ground states by external stimuli such as strain, chemical doping, electrostatic field, and magnetoelectric coupling. In summary, $Fe_{5-x}GeTe_2$ is a very promising 2D ferromagnetic platform for pursuing the state-of-the-art spintronic devices, multiferroics, and nontrivial topological spin textures based on all vdW materials at room temperature.

H.Z. and L.C. are supported by an ARO-MURI program. X.C, R.B., and R.R acknowledge support from the Quantum Materials program, funded by the U.S. Department of Energy, Basic Energy Sciences, Materials Sciences Division under Contract No. DE-AC02-05CH11231. X.H. is supported by the SRC-ASCENT center which is part of the SRC-JUMP program. R.C., J.C., and J.Y. acknowledge the support of Bakar Fellows Program at University of California, Berkeley. This research used resources of the Advanced Light Source, which is a DOE Office of Science User Facility under Contract No. DE-AC02-05CH11231. The devices were fabricated in the UC Berkeley Marvell Nanofabrication Laboratory.

[1] L. D. Casto, A. J. Clune, M. O. Yokosuk, J. L. Musfeldt, T. J. Williams, H. L. Zhuang, M.-W. Lin, K. Xiao, R. G. Hennig, B. C. Sales, J.-Q. Yan, and D. Mandrus, APL Mater. **3**, 041515 (2015).

[2] V. Carteaux, D. Brunet, and G. Ouvrard, and G., and Andre, J. Phys.: Condens. Matter **7**, 69 (1995).

[3] V.Carteaux, G. Ouvrard, J. C. Grenier, and Y. Laligant, J. Magn. Magn. Mater. **94**, 127 (1991).

[4] M. A. McGuire, H. Dixit, V. R. Cooper, and B. C. Sales, Chem. Mater. **27**, 612 (2015).

[5] I. Tsubokawa, J. Phys. Soc. Jpn. **15**, 1664 (1960).

[6] M. A. McGuire, G. Clark, S. KC, W. M. Chance, G. E. Jellison, Jr., V. R. Cooper, X. Xu, and B. C. Sales, Phys. Rev. Mater. **1**, 014001 (2017).

[7] H. Zhang, W. Wei, G. Zheng, J. Lu, M. Wu, X. Zhu, J. Tang, W. Ning, Y. Han, L. Ling, J. Yang, W. Gao, Y. Qin, and M. Tian, Appl. Phys. Lett. **113**, 072402 (2018).

[8] J. G. Checkelsky, M. Lee, E. Morosan, R. J. Cava, and N. P. Ong, Phys. Rev. B **77**, 014433 (2008).

[9] Y. Yamasaki, R. Moriya, M. Arai, S. Masubuchi, S. Pyon, T. Tamegai, K. Ueno, and T. Machida, 2D Mater. **4**, 041007 (2017).

[10] B. Chen, J. Yang, H. Wang, M. Imai, H. Ohta, C. Michioka, K. Yoshimura, and M. Fang, J. Phys. Soc. Jpn. **82**, 124711 (2013).

[11] A. F. May, S. Calder, C. Cantoni, H. Cao, and M. A. McGuire, Phys. Rev. B **93**, 014411 (2016).

[12] K. Kim, J. Seo, E. Lee, K. T. Ko, B. S. Kim, B. G. Jang, J. M. Ok, J. Lee, Y. J. Jo, W. Kang, J. H. Shim, C. Kim, H. W. Yeom, B. Il Min, B. J. Yang, and J. S. Kim, Nat. Mater. **17**, 794 (2018).

[13] D. Yuan, S. Jin, N. Liu, S. Shen, Z. Lin, K. Li, and X. Chen, Mater. Res. Express **4**, 036103 (2017).

[14] C. Gong, L. Li, Z. Li, H. Ji, A. Stern, Y. Xia, T. Cao, W. Bao, C. Wang, Y. Wang, Z. Q. Qiu, R. J. Cava, S. G. Louie, J. Xia, and X. Zhang, Nature (London) **546**, 265 (2017).

[15] B. Huang, G. Clark, E. Navarro-Moratalla, D. R. Klein, R. Cheng, K. L. Seyler, D. Zhong, E. Schmidgall, M. A. McGuire, D. H. Cobden, W. Yao, D. Xiao, P. Jarillo-Herrero, and X. Xu, Nature (London) **546**, 270 (2017).

[16] Z. Fei, B. Huang, P. Malinowski, W. Wang, T. Song, J. Sanchez, W. Yao, D. Xiao, X. Zhu, A. F. May, W. Wu, D. H. Cobden, J. H. Chu, and X. Xu, Nat. Mater. **17**, 778 (2018).

[17] D. MacNeill, G. M. Stiehl, M. H. D. Guimaraes, R. A. Buhrman, J. Park, and D. C. Ralph, Nat. Phys. **13**, 300 (2016).

[18] S. Jiang, L. Li, Z. Wang, K. F. Mak, and J. Shan, Nat. Nanotechnol. **13**, 549 (2018).

[19] S. Jiang, J. Shan, and K. F. Mak, Nat. Mater. **17**, 406 (2018).

[20] Y. Deng, Y. Yu, Y. Song, J. Zhang, N. Z. Wang, Z. Sun, Y. Yi, Y. Z. Wu, S. Wu, J. Zhu, J. Wang, X. H. Chen, and Y. Zhang, Nature (London) **563**, 94 (2018).

[21] Q. Li, M. Yang, C. Gong, R. V. Chopdekar, A. T. N'Diaye, J. Turner, G. Chen, A. Scholl, P. Shafer, E. Arenholz, A. K. Schmid, S. Wang, K. Liu, N. Gao, A. S. Admasu, S. W. Cheong, C. Hwang, J. Li, F. Wang, X. Zhang, and Z. Qiu, Nano Lett. **18**, 5974 (2018).

[22] M. Yang, Q. Li, R. V. Chopdekar, C. Stan, S. Cabrini, J. W. Choi, S. Wang, T. Wang, N. Gao, A. Scholl, N. Tamura, C. Hwang, F. Wang, and Z. Qiu, Adv. Quant. Technol. **3**, 2000017 (2020).

[23] Z. Wang, D. Sapkota, T. Taniguchi, K. Watanabe, D. Mandrus, and A. F. Morpurgo, Nano Lett. **18**, 4303 (2018).

[24] X. Wang, J. Tang, X. Xia, C. He, J. Zhang, Y. Liu, C. Wan, C. Fang, C. Guo, W. Yang, Y. Guang, X. Zhang, H. Xu, J. Wei, M. Liao, X. Lu, J. Feng, X. Li, Y. Peng, H. Wei, R. Yang, D. Shi, X. Zhang, Z. Han, Z. Zhang, G. Zhang, G. Yu, and X. Han, Sci. Adv. **5**, eaaw8904 (2019).

[25] M. Alghamdi, M. Lohmann, J. Li, P. R. Jothi, Q. Shao, M. Aldosary, T. Su, B. P. T. Fokwa, and J. Shi, Nano Lett. **19**, 4400 (2019).

[26] B. Ding, Z. Li, G. Xu, H. Li, Z. Hou, E. Liu, X. Xi, F. Xu, Y. Yao, and W. Wang, Nano Lett. **20**, 868 (2020).

[27] Y. Wu, S. Zhang, G. Yin, J. Zhang, W. Wang, Y. L. Zhu, J. Hu, K. Wong, C. Fang, C. Wang, X. Han, Q. Shao, T. Taniguchi, K. Watanabe, J. Zang, Z. Mao, X. Zhang, and K. L. Wang, arXiv:1907.11349.

[28] A. F. May, D. Ovchinnikov, Q. Zheng, R. Hermann, S. Calder, B. Huang, Z. Fei, Y. Liu, X. Xu, and M. A. McGuire, ACS Nano **13**, 4436 (2019).

[29] J. Stahl, E. Shlaen, and D. Johrendt, Z. Anorg. Allg. Chem. **644**, 1923 (2018).

[30] A. F. May, C. A. Bridges, and M. A. McGuire, Phys. Rev. Mater. **3**, 104401 (2019).

[31] J. Seo, D. Y. Kim, E. S. An, K. Kim, G.-Y. Kim, S.-Y. Hwang, D. W. Kim, B. G. Jang, H. Kim, G. Eom, S. Y. Seo, R. Stania, M. Muntwiler, J. Lee, K. Watanabe, T. Taniguchi, Y. J. Jo, J. Lee, B. I. Min, M. H. Jo, H. W. Yeom, S.-Y. Choi, J. H. Shim, and J. S. Kim, Sci. Adv. **6**, eaay8912 (2020).

[32] See Supplemental Material at http://link.aps.org/supplemental/10.1103/PhysRevB.102.064417 for additional information on Method section, XRD, magnetic properties, AFM, anomalous Hall effect, and magnetoresistance, which includes Refs. [28,29,33].

[33] Z. Li, W. Xia, H. Su, Z. Yu, Y. Fu, L. Chen, X. Wang, N. Yu, Z. Zou, and Y. Guo, arXiv:2003.06825.

[34] Y. Liu, V. N. Ivanovski, and C. Petrovic, Phys. Rev. B **96**, 144429 (2017).

[35] A. T. Ngo, P. Bonville, and M. P. Pileni, J. Appl. Phys. **89**, 3370 (2001).

[36] J. Q. Xiao, J. S. Jiang, and C. L. Chien, Phys. Rev. Lett. **68**, 3749 (1992).

[37] F. Spizzo, E. Angeli, D. Bisero, F. Ronconi, P. Vavassori, P. Allia, V. Selvaggini, M. Coisson, P. Tiberto, and F. Vinai, J. Magn. Magn. Mater. **262**, 88 (2003).

[38] P. Allia, M. Knobel, P. Tiberto, and F. Vinai, Phys. Rev. B **52**, 15398 (1995).

[39] H. Wang, C. Lu, J. Chen, Y. Liu, S. L. Yuan, S.-W. Cheong, S. Dong, and J.-M. Liu, Nat. Commun. **10**, 2280 (2019).